

Real-space structure of the impurity screening cloud in the Resonant Level Model

Shreyoshi Ghosh¹, Pedro Ribeiro^{1,2}, and Masudul Haque¹

¹ Max-Planck-Institut für Physik komplexer Systeme, Nöthnitzer Straße 38, D-01187 Dresden, Germany

² Centro de Física das Interações Fundamentais, Instituto Superior Técnico, Universidade de Lisboa, Av. Rovisco Pais, 1049-001 Lisboa, Portugal

Abstract.

We present a detailed investigation of the impurity screening cloud in the Resonant Level Model. The screening is visible in the structure of impurity-bath correlators as a function of distance from the impurity. We characterize the screening cloud through scaling analyses of impurity-bath correlators and entanglement entropies. We devise and study several situations where the screening cloud is destroyed or modified: finite temperatures, energetic detuning of the impurity from the chemical potential, and the situation of an unconventional bath with diverging density of states.

1. Introduction

The concept of a “Kondo screening cloud” has caused much discussion and controversy in the field of quantum impurity physics. Single-impurity models generally possess an emergent energy scale. The most famous is perhaps the celebrated Kondo temperature for the single-impurity Kondo model, [1, 2] but similar energy scales appear in the single-impurity Anderson model [2, 3] and the interacting resonant level model [4, 5]. There is a length scale ξ corresponding to this energy scale, which suggests that the bath surrounding the impurity is affected differently at distances less than ξ from the impurity than at larger distances $x > \xi$, i.e., there should be a screening cloud of radius ξ surrounding the impurity.

Although the impurity screening cloud is difficult to observe directly experimentally, calculations have shown that this impurity lengthscale does in fact appear in real-space properties of the bath. The properties (e.g., persistent current or conductivity) of a mesoscopic device containing a Kondo or Anderson impurity has been found to behave differently if the device size is larger or smaller than the size of the Kondo cloud [6, 7, 8, 9, 10]. Numerical and variational calculations have found real-space properties (e.g., impurity-bath correlation functions, distortion of local density of states, entanglement properties, etc) to be different for $x < \xi$ and $x > \xi$ [11, 12, 13, 14, 15, 16, 17, 18, 19, 20], for Anderson and Kondo models and for spin-chain versions of the Kondo model. These recent results support earlier perturbative calculations of real-space structure [21, 22, 23].

In this work, we focus on the screening cloud around the impurity in the resonant level model (RLM):

$$H_{\text{RLM}} = \sum_k \epsilon_k c_k^\dagger c_k - \frac{J'}{\sqrt{\mathcal{L}}} \sum_k (d^\dagger c_k + c_k^\dagger d) + \epsilon_d d^\dagger d. \quad (1)$$

where c_k, c_k^\dagger are the bath fermion operators at momentum k and d, d^\dagger are the fermion operators at the impurity site, ϵ_k is the dispersion of the bath fermions, J' is the hopping strength between impurity and position $x = 0$ of the bath, \mathcal{L} is the bath size, and the on-site potential ϵ_d is generally tuned to the bath chemical potential. Here x represents the distance from the impurity. Our results are mainly for one-dimensional (1D) baths, but much of the discussion is expected to be valid for any dimensionality. For small J' , the RLM possesses a small energy scale and correspondingly a large length scale, depending as $(J')^{-2}$ on the coupling. In this article we analyze the real-space structure appearing at such length scales.

The resonant level model appears as solvable limits of the interacting resonant level model (IRLM) [4], the single-impurity Anderson model (SIAM) [3, 2], and the anisotropic Kondo model [2, 25]. Each of these impurity models have a known energy scale and associated length scale. The IRLM, $H_{\text{IRLM}} = H_{\text{RLM}} + V d^\dagger d c_{x=0}^\dagger c_{x=0}$, has an impurity-bath interaction V . The length scale is known to depend on J' as a power law, $J'^{-\alpha(V)}$, with the interaction-dependent exponent $\alpha(V)$ taking the value $\alpha(0) = 2$ at the RLM point [4, 5]. The SIAM contains two copies (spins \uparrow and \downarrow) of the RLM,

with an on-site interaction U between the two spin species. The SIAM has an emergent energy/length scale [24] and the appearance of this scale in the spatial dependence of correlation functions have been explored in Ref. [14].

For the isotropic Kondo model, the energy scale is the Kondo temperature, given by the well-known expression $T_K = D \exp[-1/\rho(\varepsilon_F)J_K]$. (Here J_K is the Kondo coupling, $\rho(\varepsilon_F)$ is density of states of the conduction electrons at fermi energy and D is the band width.) The spatial behavior of the impurity-bath spin-spin correlator has been explored earlier in Refs. [22, 21, 23] and more recently in Refs. [15, 16]. The expression for the energy scale is considerably more complicated for anisotropic Kondo couplings, but becomes simpler at a special value of the anisotropy called the Toulouse point [2, 25]. At the Toulouse point, the Kondo model can be mapped to the non-interacting RLM. Because of solvability, the Toulouse point is widely used in many studies of Kondo physics. For example, it has been used for non-equilibrium calculations for Kondo impurities [26, 27, 28, 29]. Spatial structures in the bath have been studied for the Toulouse point in Ref. [30] for helical edge states serving as baths, and in Ref. [28] in the context of time evolution.

Our work belongs to this general theme of exploring emergent length scales in impurity models through the study of real-space profiles. We concentrate primarily on the spatial dependence of the two-point impurity-bath correlator $\langle d^\dagger c_x \rangle$, i.e., the equal-time Greens function or the one-body density matrix. This is the natural analog, for the RLM, of the impurity-bath spin-spin correlator $\langle \vec{S}_{\text{imp}} \cdot \vec{s}_x \rangle$ commonly used in studies of the screening cloud in the Kondo and Anderson models [15, 14, 16, 13].

We present analytic expressions for the model as written in Eq. 1, and numerical calculations for specific lattice implementations. The lattices are described in Section 2. We find the structure of the screening cloud to be very similar for various lattice geometries, in contrast to some other impurity situations (spin chains, persistent currents through rings) where the physics can depend markedly on impurity geometry [31, 7].

The correlator $\langle d^\dagger c_x \rangle$ has oscillations with period equal to the Fermi wavevector k_F . As in Ref. [15], the structure of the screening cloud is seen by analyzing the envelope of these oscillations. The analytic expressions for $\langle d^\dagger c_x \rangle$ presented in Section 3 show clearly different behaviors for $x < \xi$ and $x > \xi$; the envelope depends logarithmically on distance within the screening cloud and shows the expected Fermi liquid behavior $\sim x^{-1}$ at larger distances. The width of the spectral function scales as J'^2 ; we identify this energy/temperature as the RLM analog of the Kondo temperature. From these results, with relatively mild assumptions, one can predict also aspects of the structure of the Kondo cloud in the SIAM (Section 3.1).

In numerical calculations on finite lattices (Section 4), boundary effects modify the cloud shape in geometry-dependent ways. To see the crossover from $-\ln x$ to $1/x$ behavior clearly at reasonable system sizes, we have combined multiple values of the coupling J' . The data sets show good scaling collapse.

In Section 5 we show what happens to the screening cloud when the impurity level

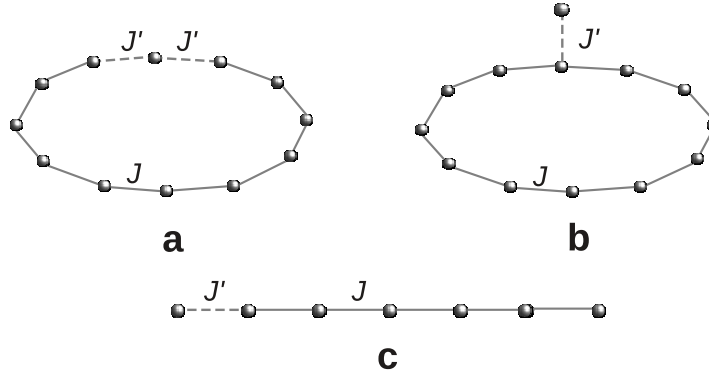


Figure 1. Geometries used for lattice realizations of the RLM. The impurity site can be (a) Embedded, (b) extrenal, or (c) end-coupled.

energy (ϵ_d) is detuned away from the chemical potential. The detuning induces an intermediate region in the spatial profile of $\langle d^\dagger c_x \rangle$, which gradually encroaches toward smaller distances with increasing detuning and destroys the $-\ln x$ behavior within the Kondo cloud.

In Section 6 we characterize the screening cloud using the quantum entanglement of a region of size ℓ containing the impurity with the rest of the bath. Unlike $\langle d^\dagger c_x \rangle$, we do not have analytic predictions for the size dependence of the block entanglement entropy, but the numerically determined entanglement shows clear ℓ/ξ scaling.

In Section 7 we engineer an unconventional bath that has a divergent density of states at the Fermi energy, due to part of the dispersion being not linear but quadratic at the Fermi surface. The resulting screening involves an additional scale, and the long-distance power-law decay of $\langle d^\dagger c_x \rangle$ now has a “non-Fermi-liquid” exponent.

2. Lattice geometries: embedded, external, and endpoint impurities

The RLM, given in Eq. (1), describes the resonance of an impurity level tunnel-coupled to a bath of spinless fermions (“conduction electrons”). We will use 1D tight-binding lattices of non-interacting fermions to realize the conduction bath. The impurity level at site i_{imp} is coupled to this bath with a hopping strength J' much weaker than the hopping J within the bath. As shown in Figure 1, we consider three different geometries (locations of i_{imp}): (a) embedded, (b) external, and (c) end-coupled RLMs. The Hamiltonians describing these three geometries are:

$$H_{emb} = -J \left[\sum_{i=-L}^{-2} + \sum_{i=1}^L \right] (c_i^\dagger c_{i+1} + \text{h.c.}) - J' \left[(c_1^\dagger d + c_{-1}^\dagger d) + \text{h.c.} \right] \quad (2)$$

$$H_{ext} = -J \sum_{i=-L+1}^{L-1} (c_i^\dagger c_{i+1} + \text{h.c.}) - J' (c_0^\dagger d + \text{h.c.}). \quad (3)$$

$$H_{end} = -J \sum_{i=1}^{L-1} (c_i^\dagger c_{i+1} + \text{h.c.}) - J' (d^\dagger c_1 + \text{h.c.}) \quad (4)$$

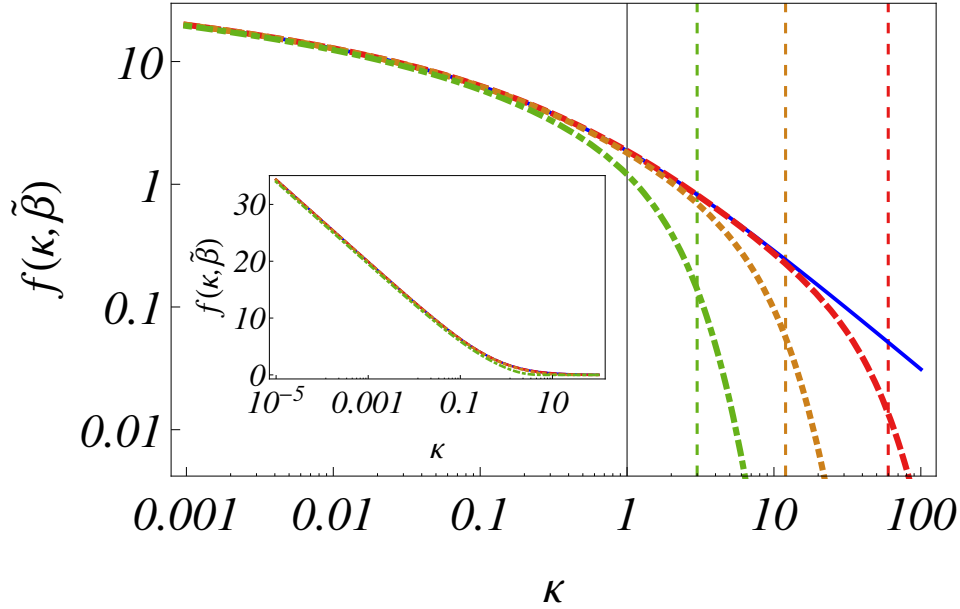


Figure 2. Scaled envelope of two-point correlator $f(\kappa, \tilde{\beta})$ (defined in Eqs. 8,9) as a function of scaled distance κ , in log-log scale. We show both zero temperature (blue solid line) and finite temperatures: $\tilde{\beta} = 60$ (red dashed line), $\tilde{\beta} = 12$ (orange dotted line), $\tilde{\beta} = 3$ (green dash-dotted line). The $\kappa = 1$ vertical line indicates the crossover lengthscale (size of screening cloud). The finite-temperature curves deviate sharply from $f(\kappa)$ at distances larger than $\kappa = \tilde{\beta}$ (shown with dashed lines for the three $\tilde{\beta}$ values). Inset: $f(\kappa)$ plotted in log-linear scale. The $-\ln \kappa$ behavior within the cloud ($\kappa < 1$) is clear from the constant slope.

The impurity site is located at $i_{imp} = 0$ for embedded and end-coupled RLMs ($d \equiv c_0$). In the external RLM, it is located at an external site and couples only to site $i = 0$ of the chain. The total system size (bath+impurity) is $\mathcal{L} = 2L + 1$, $2L$ and L for embedded, external and end-coupled geometries respectively. For embedded and external RLMs, one could choose either periodic or open 1D chains; we work with periodic chains. For infinite chains or with open boundary conditions, the embedded Hamiltonian can be mapped onto the endpoint Hamiltonian with a rescaled J' .

We will restrict to half-filling, which corresponds to zero chemical potential. The Hamiltonians above are written for the case where the impurity level is tuned to the chemical potential, $\epsilon_d = 0$, and hence the $\epsilon_d d^\dagger d$ term is omitted. The effect of a detuning term will be explored in Section 5.

3. Two-point correlator: analytic results

In this section we present the essential features of the screening cloud using analytic results for the $\langle d^\dagger c_x \rangle$ correlator. This can be derived at finite temperature using standard means, yielding:

$$\langle d^\dagger c_i \rangle = -J' \frac{1}{L} \sum_k \int d\nu A_{dd}(\nu) \frac{n_f(\nu) - n_f(\varepsilon_k - \mu)}{\nu - (\varepsilon_k - \mu)} e^{-ikr_i}, \quad (5)$$

where $A_{dd}(\nu)$ is the spectral function of the impurity and $n_f(\nu) = 1/(1 + e^{\beta\nu})$ is the Fermi function at temperature $T = 1/\beta$. For completeness we provide explicit details of the derivation of Eq.(5) in the Appendix.

Assuming that the dispersion relation of the bath electrons remains linear within an energy window Λ around the Fermi level, i.e., $(\epsilon_k - \mu) \simeq v_F (|k| - k_F)$ for $|\epsilon_k - \mu| \lesssim \Lambda$, and that $T/\Lambda, \Gamma/\Lambda \ll 1$ (where Γ is the characteristic energy broadening of the impurity spectral function), Eq.(5) can be approximated by

$$\langle d^\dagger c_i \rangle = -\frac{J'\rho_0}{\pi} \text{Re} \left[e^{ik_F r_i} \int d\varepsilon \int d\nu A_{dd}(\nu) \frac{n_f(\nu) - n_f(\varepsilon)}{\nu - \varepsilon} e^{i\frac{\varepsilon r_i}{v_F}} \right]. \quad (6)$$

In line with the above approximations the density of states of the bath electrons in the absence of the coupling is taken to be constant within the Λ -window: $\rho(\nu) \simeq \rho_0 \Theta(\Lambda - |\nu - \mu|)$.

For the RLM in the wide-band limit the impurity spectral function can be approximated by

$$A_{dd}(\nu) = \frac{1}{\pi} \frac{\Gamma}{(\nu - \epsilon_d + \mu)^2 + \Gamma^2}, \quad (7)$$

with $\Gamma = \pi J'^2 \rho_0$ corresponding to the hybridization width (see Appendix). In the following we assume that the resonance condition $\epsilon_d = \mu$ is always fulfilled. In this case Eq. (6) further simplifies to

$$\langle d^\dagger c_i \rangle = \frac{J'\rho_0}{\pi} \text{Re} \left[e^{ik_F r_i} f(\kappa, \tilde{\beta}) \right] \quad (8)$$

where $\kappa = \frac{r_i}{\xi}$, $\xi = \frac{v_F}{\Gamma}$, $\tilde{\beta} = \frac{\Gamma}{T}$, and with f given by

$$f(\kappa, \tilde{\beta}) = \pi \int_{-\infty}^{\infty} dx \frac{x \cos(\kappa x) + \sin(\kappa x)}{(x^2 + 1)(1 + e^{\tilde{\beta} x})} \quad (9)$$

At zero temperature, defining $f(\kappa) = f(\kappa, \beta \rightarrow \infty)$, one obtains the asymptotic forms

$$f(\kappa) \simeq -\frac{\pi}{\kappa}; \quad \kappa \rightarrow \infty \quad (10)$$

$$f(\kappa) \simeq -\pi [\ln(\kappa) + \gamma]; \quad \kappa \rightarrow 0 \quad (11)$$

with γ the Euler constant. The scaling function $f(\kappa, \tilde{\beta})$ is plotted in Figure 2. For finite $\tilde{\beta}$ one can identify $\kappa_T = \tilde{\beta}$ such that $f(\kappa, \tilde{\beta}) \simeq f(\kappa)$ for $\kappa \ll \kappa_T$.

We note that the broadening of the spectral function, $\Gamma = \pi \rho_0 J'^2$, acts as the characteristic energy scale. We therefore identify this as the analog of the Kondo temperature for the RLM, and denote it as T_{SC} to highlight the connection to screening cloud formation. The characteristic length scale is $\xi = v_F/T_{SC}$.

3.1. Implications for the Anderson model

As it stands, Eq. (5) is valid not only for the RLM but also for the Anderson impurity model. Thus we have a prediction for the correlators $\langle d_\sigma^\dagger c_{x\sigma} \rangle$ in the SIAM. (Here σ is \uparrow or \downarrow .) If Γ_{SIAM} is the broadening of the spectral function in the SIAM, the behavior of this correlator will be $\sim -\ln(x/\xi_{SIAM})$ for $x < \xi_{SIAM}$ and $\sim x^{-1}$ for $x > \xi_{SIAM}$, where

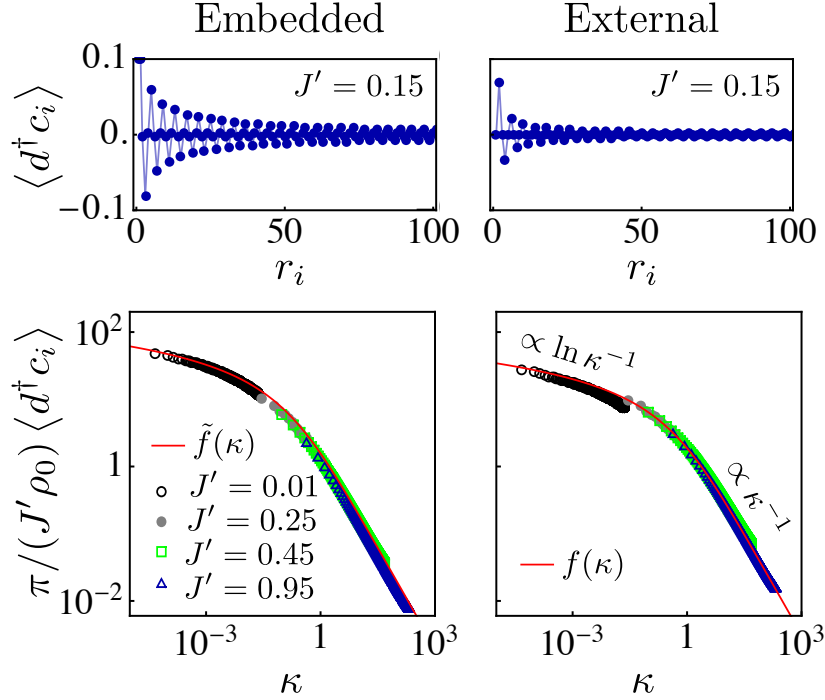


Figure 3. Upper panels: Correlator $\langle d^\dagger c_i \rangle$ plotted against distance r_i from the impurity site for finite-size RLM systems in the embedded and external geometries. System sizes and number of particles are $\mathcal{L} = 2003$, $N = 1001$ for the embedded and $\mathcal{L} = 2000$, $N = 1000$ for the external geometries. Lower panels: Scaled envelope of $\langle d^\dagger c_i \rangle$ against scaled distance κ plotted for different values of J' . The external case (right) is compared with $f(\kappa)$ function. The embedded case (left) is compared with $\tilde{f}(\kappa) \simeq 2.0f(3.2\kappa)$.

$\xi_{SIAM} = v_F/\Gamma_{SIAM}$. One expects these functional forms to hold at low temperatures, even if the spectral function is not an exact Lorentzian and even if the spectral function has temperature dependence.

The correlator usually used for describing the screening cloud for the Anderson model is not $\langle d^\dagger_\sigma c_{x\sigma} \rangle$ but the spin-spin correlator [13, 14]. For $U = 0$, Wick's theorem implies this to be proportional to the square of $\langle d^\dagger_\sigma c_{x\sigma} \rangle$. Thus we can expect $\langle \vec{S}_{\text{imp}} \cdot \vec{s}_x \rangle$ to behave like $[\ln x - \ln \xi_{SIAM}]^2$ within the screening cloud for small values of U . We have found that the data in Ref. [13] is qualitatively consistent with this prediction for interactions as large as $U \sim 2$.

4. Two-point correlators on finite-size lattice RLM's

In this section we present numerical results for the equal-time correlator $\langle d^\dagger c_i \rangle$ characterizing the spatial structure of the screening cloud in RLMs on finite chains of length \mathcal{L} for the three geometries introduced in Section 2 at zero and finite temperature. The analytic predictions of Section 3 are directly applicable to the external geometry, but we will show that the predicted scaling matches the end-coupled and embedded

cases with the use of simple scaling factors. Boundary effects are found to be different for the three geometries.

For our numerical calculations we consider systems of size $\simeq 10^3$ at half-filling with even (odd) number of total lattice sites for end-coupled and external (embedded) RLMs.

4.1. Zero temperature

The single-particle correlation functions $\langle d^\dagger c_i \rangle$, at temperature $T = 0$, are shown in Figure 3 for different geometries. The correlators oscillate as $\sim \cos(k_F r_i)$ with distance r_i from the impurity site. Since we are at half-filling, the Fermi momentum k_F is commensurate with the lattice spacing, so the envelope of oscillations can be obtained by plotting $|d^\dagger c_{(i=2n)}|$, where n is an integer. The lower row of Figure 3 shows the envelopes obtained in this way.

For these sizes ($\simeq 10^3$), the envelope for a single value of J' follows only a small part of the scaling curve $f(\kappa)$. These individual curves show finite-size deviations near the system boundaries. The curves for many J' together reconstruct very well the full scaling curve $f(\kappa)$ for the external geometry. For the embedded and end-point geometries the scaling collapse still occurs, but the scaling function and its argument have to be rescaled, $\tilde{f}(\kappa) = Af(c\kappa)$.

The collapse of the envelopes for different J' onto the single curve confirms the existence of the finite screening length scale ξ in all three realizations of RLMs, conjectured from analytical calculation for the external RLM.

For small J' ($= 0.01J$), the screening length ξ is much larger than the system size \mathcal{L} and the r_i^{-1} behavior of the free-fermionic correlator is absent as the impurity is not completely screened within the length of the system. On the other hand, for large J' ($= 0.95J$), $\xi \ll \mathcal{L}$ and the correlation function behaves mostly as r_i^{-1} as the impurity gets screened over a very small distance.

4.2. Logarithm versus power law within the screening cloud

In the isotropic Kondo model, impurity-bath spin-spin correlators have been reported to show a crossover, at the screening length-scale, between power-law behaviors of different exponents [15]. In contrast, in the RLM, the correlator does not become a power-law of smaller exponent within the screening cloud, but rather becomes a logarithm. We highlight this in Figure 4 by plotting the logarithmic derivative $\partial \ln \langle d^\dagger c_i \rangle / \partial (\ln \kappa)$ as a function of κ from the numerical data for all three geometries. We also compare with the analytical predictions.

When the dependence is a power-law, the logarithmic derivative is the corresponding exponent. Therefore it converges to -1 at large distances. At small distances within the screening cloud ($\kappa < 1$), the logarithmic derivative increases continuously toward zero as κ decreases.

The numerical curves for each J' shows finite size effects as the system boundary is approached, but otherwise the curves collapse onto the analytical prediction in the

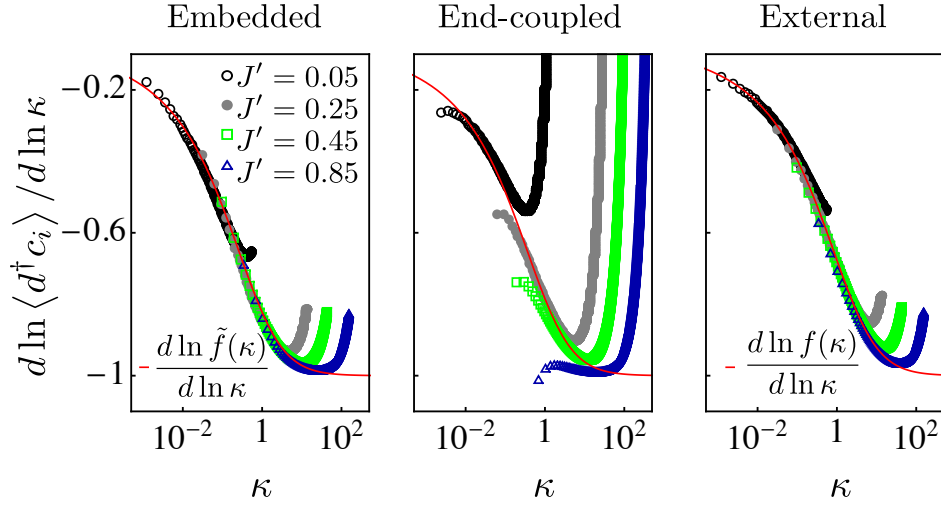


Figure 4. Plot of logarithmic derivative $d \ln \langle d^\dagger c_i \rangle / d \ln \kappa$ as a function of κ for embedded, end-coupled and external RLMs. For the external case the solid (red) line corresponds to the derivative of $\ln f(\kappa)$ obtained from analytical calculation. For the other two cases the envelope is seen to behave as $Af(c\kappa)$ with A and c constants of order 1. The fitted values of c are $c \simeq 3.2$ (embedded) and $c \simeq 2.3$ (end-coupled). The system sizes \mathcal{L} are same as in Fig. 3

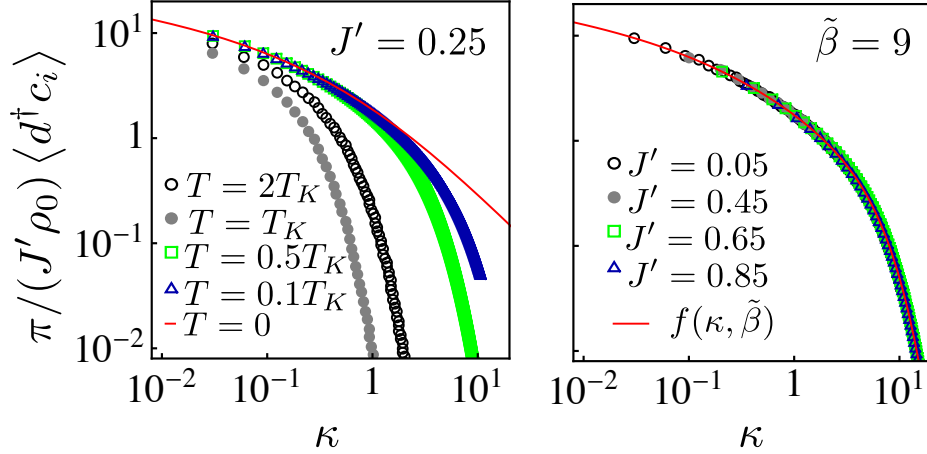


Figure 5. Envelope of the correlation function $\langle d^\dagger c_i \rangle$ plotted against the scaled distance κ . Left panel: Fixed $J' = 0.25J$ and different values of the temperature. The solid (red) line corresponds to $f(\kappa)$. Right panel: Fixed rescaled temperature $\tilde{\beta} = 9$ and different values of J' . The solid (red) line corresponds to $f(\kappa, \tilde{\beta} = 9)$.

external case. In the other two geometries the rescaled form $\tilde{f}(\kappa) = Af(c\kappa)$ has to be used.

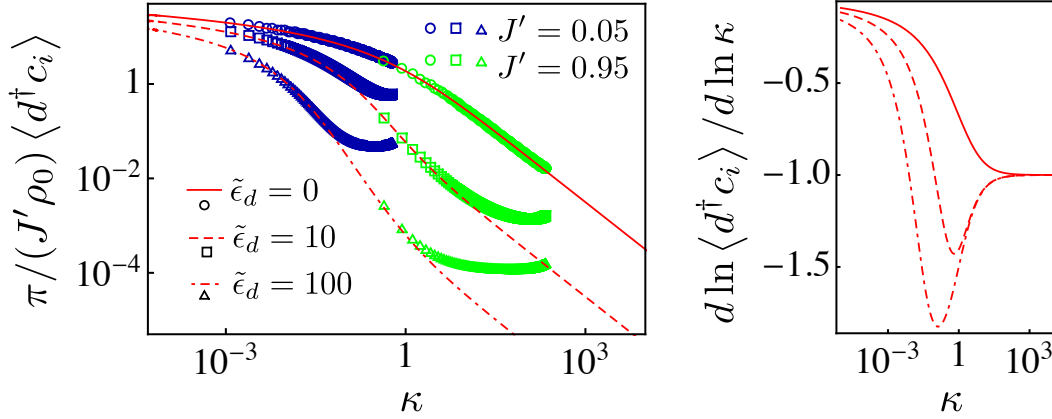


Figure 6. Effect of mismatch ϵ_d between impurity site energy and bath chemical potential. Left: Scaled envelope of $\langle d^\dagger c_i \rangle$ as a function of κ for $\tilde{\epsilon}_d = 0, 10, 100$. Full curves show analytic function $f(\kappa, \tilde{\epsilon}_d)$, while the dots are numeric data for $\mathcal{L} = 2000$. The full scaling curve can be constructed with a combination of several J' values; here we show only two values. Right: Plot of logarithmic derivative of $f(\kappa, \tilde{\epsilon}_d)$ with same values of $\tilde{\epsilon}_d$ as in left panel.

4.3. Finite temperature

Next, we consider the correlation functions at finite temperature. The screening length ξ corresponds to the temperature scale $T_{SC} = v_F/\xi$, above which the screening of impurity by conduction electrons is thermally destroyed. In Fig.5-(left), the envelope of oscillations are shown for the external geometry, for several different temperatures. Finite temperature induces another length scale $\xi_T = v_F/T$, the thermal length scale. The behavior of $\langle d^\dagger c_i \rangle$ is not much affected by the temperature in regions $r_i < \xi_T$ while it shows an exponential decay $\sim e^{-r_i/\xi_T}$ for $r_i > \xi_T$. Plots of the rescaled envelope as a function of κ , keeping $\tilde{\beta} = T_{SC}/T$ fixed, shown in Fig.5-(right), confirm the predicted scaling form $f(\kappa, \tilde{\beta})$ of the correlator. In Fig.5 we present finite temperature numerical results only for the external RLM. Similar features are observed in the other two geometries.

5. RLM with on-site potential

So far we have considered the on-site energy of the impurity level ϵ_d to be the same as the chemical potential $\mu = 0$ of the fermionic bath. In this section we consider the effect of finite ϵ_d on the screening cloud. We focus on the external RLM at half-filling and zero temperature; the relevant Hamiltonian is $H_{ext} + \epsilon_d d^\dagger d$.

The analytical expression for $\langle d^\dagger c_i \rangle$ in the presence of impurity detuning can be obtained using the Green's function method described in Section 3:

$$\langle d^\dagger c_i \rangle = \frac{J' \rho_0}{\pi} \text{Re} [e^{ik_F r_i} f(\kappa, \tilde{\epsilon}_d)] \quad (12)$$

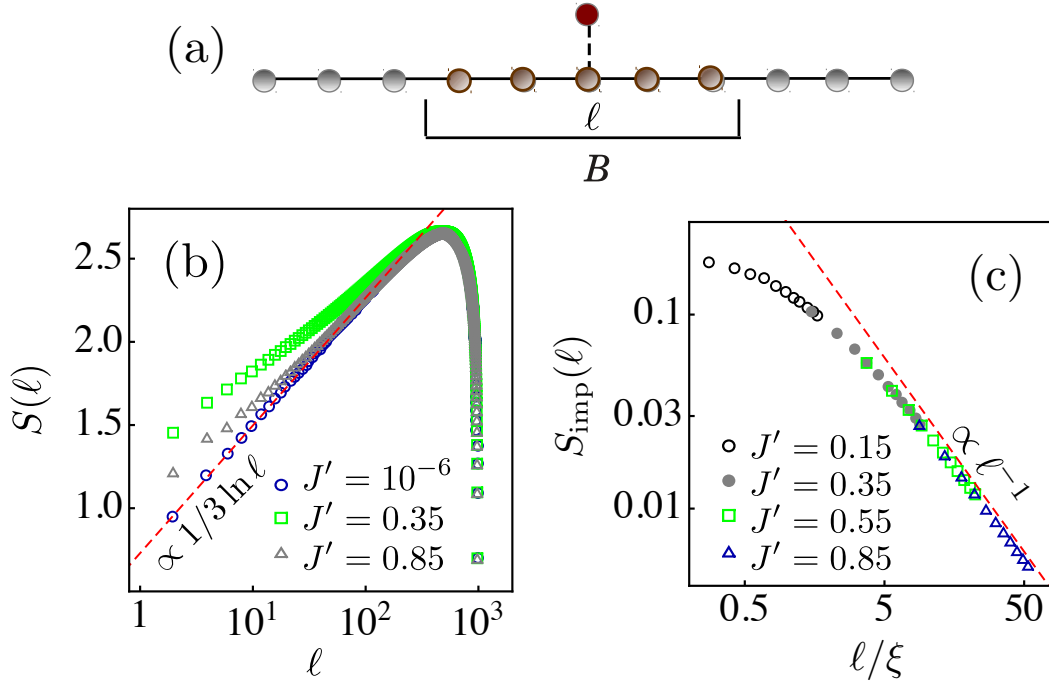


Figure 7. (a) Schematic diagram of subsystem B of length ℓ , including the impurity site in external RLM. (b) Entanglement entropy $S(\ell)$ between subsystem B and the rest as a function of subsystem size ℓ for $\mathcal{L} = 1000$ and several J' values. For very small $J' = 10^{-6}J$, one observes the expected logarithmic behavior $S(\ell) \simeq \frac{1}{3} \ln \ell + \text{const.}$ for $\ell \ll \mathcal{L}$. (c) Impurity entanglement entropy $S_{\text{imp}} = S - S_{J'=0}$ as a function of ℓ/ξ for several values of J' , keeping the value of ℓ/\mathcal{L} fixed to $1/4$. A scaling collapse is observed for different values of J' . For large ℓ , S_{imp} vanishes as ℓ^{-1} .

where

$$f(\kappa, \tilde{\epsilon}_d) = \pi \int_{-\infty}^0 dx \frac{e^{i\kappa x}}{x - \tilde{\epsilon}_d + i} \quad (13)$$

Here $\tilde{\epsilon}_d = \epsilon_d/\Gamma$ is the scaled impurity energy. A plot of this analytical function together with numerical results are shown in Figure 6-(left). The κ^{-1} behavior of the correlation function is still present for regions $\kappa > 1$ outside the cloud. However, another region, with non-logarithmic behavior, develops within the cloud ($\kappa < 1$). This region expands from the exterior of the cloud towards its center at the impurity site and increases with increasing ϵ_d , thus destroying the characteristic logarithmic behavior of the screening cloud. The loss of the logarithmic region is highlighted in Figure 6-(right) using the logarithmic derivative.

6. Entanglement entropy

Having characterized the screening cloud using impurity-bath correlators in most of this work, in this section we focus on a different quantity. We consider the entanglement entropy of a subsystem (B) of length ℓ , including the impurity site at its center, with

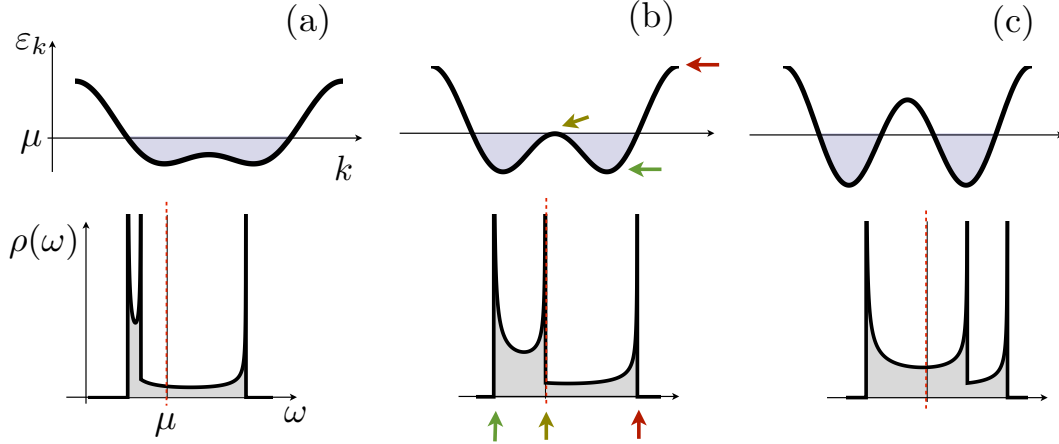


Figure 8. Dispersion relations and the respective densities of states, for three cases with different Fermi surface geometry. The cases shown correspond to the Hamiltonian H_{NN} of Eq. (17) with $J' = 0$ and: (a) $J_{NN} = -0.5J$; (b) $J_{NN} = -J$; (c) $J_{NN} = -3J$. The finite density of states at the Fermi level of cases (a) and (c) induces the scaling of $\langle d^\dagger c_i \rangle$ given in Eqs. (8,9). For case (b) where $\rho(\omega \rightarrow \mu) \propto |\omega|^{-1/2} \Theta(-\omega)$ the impurity cloud follows Eqs. (15,16).

the rest of the system (A). The entanglement entropy is defined as $S = -\text{Tr}_B[\rho_B \ln \rho_B]$, where $\rho_B = \text{Tr}_A \rho$ is the reduced density matrix of subsystem B , obtained by tracing over the A degrees of freedom. For free fermionic systems like the RLM, the entanglement entropy can also be expressed as $S = -\sum_i [\nu_i \ln \nu_i + (1 - \nu_i) \ln (1 - \nu_i)]$, where ν_i 's are the eigenvalues of one particle correlator $[C_{ij}] = [\langle c_i^\dagger c_j \rangle]$, $i, j \in B$.

As shown in Ref. [19] for spin chains, such block entanglement entropies exhibit signatures of the screening length scale. The impurity entanglement entropy is defined as

$$S_{\text{imp}}(\ell) = S(\ell) - S_{J'=0}(\ell). \quad (14)$$

This quantity is expected to follow a scaling form, i.e. to depend only on the ratio ℓ/ξ , provided that ℓ/\mathcal{L} is constant or $\ell \ll \mathcal{L}$.

We present here the numerical results for entanglement entropy of external RLM; the entanglement entropy for endpoint/embedded geometries has very similar features and has been presented recently in Ref. [32]. Fig. 7-(b) shows $S(\ell)$ for several values of J' . For $J' = 0$, which corresponds to the system without impurity, the entanglement entropy has the form $S_{J'=0}(\ell) = \frac{1}{3} \ln \ell + \text{const.}$ for $\ell \ll \mathcal{L}$, confirming the prediction from conformal field theory with central charge $c = 1$. Fig. 7-(c) shows $S_{\text{imp}}(\ell)$ as a function of the scaled variable ℓ/ξ for different values of J' , keeping ℓ/\mathcal{L} fixed at $1/4$. The data for different J' collapses onto a single curve.

7. "Non-Fermi liquid" behaviour from an unconventional bath

The treatment of section 3 is for a single set of Fermi points such as the case shown schematically in Fig.8-(a). This analysis can be generalised to the case of multiple sets

of Fermi points such as the case shown in Fig.8-(c). In this case the envelope of the impurity cloud still follows the scaling form of Eq.(9) with the density of states getting a contribution from each one of the Fermi point pairs: $\rho_0 \simeq \pi^{-1}(|v_{F,1}|^{-1} + |v_{F,2}|^{-1})$, where $v_{F,i}$ is the velocity at Fermi point i . We assume a parity symmetric dispersion relation $\varepsilon_k = \varepsilon_{-k}$.

A qualitatively different behaviour is obtained when the density of states at the Fermi level diverges, a situation that may occur when the 1D Fermi "surface" changes its topology. Fig. 8(b) shows this situation arising at the transition between cases (a) and (c). In this section we extend our analysis to such a case. We show below that with such an unconventional bath the asymptotic behavior of the correlator $\langle d^\dagger c_i \rangle$ is qualitatively different from the regular Fermi liquid expectation κ^{-1} . The nature of this bath also introduces a new length/energy scale.

In a situation like Fig. 8(b), there is a momentum value, assumed without loss of generality to be $k = 0$, where the dispersion relation is quadratic: $|\epsilon_k - \mu| \simeq a_F k^2$. It follows that the density of states of the fermionic bath diverges as $\rho(\omega \rightarrow \mu) \simeq 1/(4\pi) |a_F(\omega - \mu)|^{-1/2} \Theta(\mu - \omega) + \rho_0$ (see Fig.8 (b) lower panel) where $\rho_0 = 1/(\pi|v_F|)$ is the contribution from the regular Fermi points. The derivation of the correlator $\langle d^\dagger c_i \rangle$ follows closely the one of case (a) (further details are provided in the Appendix) and yields

$$\langle d^\dagger c_i \rangle = \frac{J' \rho_0}{\pi} g(\kappa, s) \quad (15)$$

with $s = v_F/\sqrt{\Gamma a_F}$. The scaling function g is given by

$$g(\kappa, s) = \text{Re} \left[e^{ik_F r_i} \int_0^\infty dy \left\{ \frac{e^{-i\kappa y} \Gamma(0, -iy\kappa) \left(1 + \frac{s}{2\sqrt{y}}\right)}{y^2 + \left(1 + \frac{s}{2\sqrt{y}}\right)^2} + \frac{e^{i\kappa y} \Gamma(0, iy\kappa)}{\left(y - \frac{s}{2\sqrt{y}}\right)^2 + 1} \right\} + \pi s \int_0^\infty du \frac{e^{-us\kappa}}{\left(u^2 - \frac{s}{2u}\right)^2 + 1} \right] \quad (16)$$

with $\Gamma(a, z)$ the incomplete gamma function. Note that $g(\kappa, s)$ reduces to $f(\kappa)$ in Eq.(9) for $s = 0$. The dimensionless parameter s quantifies the effect of the diverging density of states.

For finite s the function $g(\kappa, s)$ is composed of two different contributions arising from the regular Fermi points (first term inside the square brackets in Eq.16) and from the special point at $k = 0$ (second term inside the square brackets).

For very small values of $s \neq 0$ the contribution from the second term in Eq.(16) is negligible. The envelope of the correlator $g(\kappa, s)$ exhibits three different scaling regions (see Fig. 9 - left panel) arising only from the first term:

- (i) $g(\kappa, s) \propto -\ln \kappa$ for $\kappa \ll 1$,
- (ii) $g(\kappa, s) \propto \kappa^{-1}$ for $1 \ll \kappa \ll s^{-2}$, and
- (iii) $g(\kappa, s) \propto \kappa^{-3/2}$ for $\kappa \gg s^{-2}$.

The intermediate $\sim \kappa^{-1}$ region is barely visible for $s = 10^{-2}$ (Fig. 9) but becomes clearer and more extended at even smaller s .

For large s , the contribution from the special ($k = 0$) point is large and shows a crossover from a logarithmic $g(\kappa, s) \propto \ln s\kappa$ to power-law dependence $g(\kappa, s) \propto (s\kappa)^{-3}$. The first term in Eq.(16) also shows two different scaling behaviors: $g(\kappa, s) \propto \ln \kappa$ for small κ and $g(\kappa, s) \propto \kappa^{-3/2}$ for large κ . As a result the scaling function $g(\kappa, s)$, composed of these two contributions, does not show the κ^{-3} behavior as the logarithmic dependence coming from the first term overcomes this faster decaying power-law. One then finds three different scaling regions for large values of s (Fig. 9 left panel):

- (i) $g(\kappa, s) \propto (-\ln \kappa + c_1 \ln s)$ for $\kappa \ll s^{-4/3}$,
- (ii) $g(\kappa, s) \propto -\ln \kappa$ for $s^{-4/3} \ll \kappa \ll s^{-2/3}$, and
- (iii) $g(\kappa, s) \propto \kappa^{-3/2}$ for $\kappa \gg s^{-2/3}$.

The first and second regions both have dominant $-\ln \kappa$ behaviors, but they are shifted by a constant $\sim \ln s$. This shift is visible (Fig. 9 left panel) as a jump between the two regions, around $\kappa \sim s^{-4/3}$.

In order to illustrate our analytical findings we consider a minimal model with next nearest neighbor hopping of the lattice electrons:

$$H_{NN} = H_{ext} - J_{NN} \sum (c_i^\dagger c_{i+2} + h.c.) \quad (17)$$

where the filling fraction is determined by fixing the chemical potential at $\mu = 0$ and the dispersion relation at $J' = 0$ is given by $\varepsilon_k = -2J \cos k - 2J_{NN} \cos 2k$. Depending on next nearest neighbor hopping parameter J_{NN} the energy spectrum of the bath can be categorized in three different cases as shown in Fig.8 : (a) for $-J_{NN} < J$, (b) for $-J_{NN} = J$, (c) for $-J_{NN} > J$.

Fig.9 shows $\langle d^\dagger c_i \rangle$ computed for the (b) case with $J = -J_{NN} = 1$ and $J' = 0.25J$. The regular Fermi momentum situated at $k_F = 2\pi/3$ sets an oscillatory behaviour in real space with period 3. This is visible in Fig.9-right panel as three branches. This set of parameters corresponds to $s \approx 27.3$. The numerical data is in excellent agreement with $\langle d^\dagger c_i \rangle$ calculated from Eq.(16) with $s = 27.3$ (Fig.9-right, open green points).

The envelope of the correlator can be obtained considering $\langle d^\dagger c_i \rangle$ for $i = 3n$ (with n integer) in the same spirit as in section 3. The numerically obtained envelope and the analytic prediction are shown in the inset of Fig.9-right to follow the predicted $\kappa^{-3/2}$ asymptotic behavior.

8. Higher dimensional baths

For a resonant level embedded in an electronic bath of dimensionality $D > 1$, the angular dependence of the Fermi surface has to be taken into account. In general, a higher-dimensional Fermi surface will be anisotropic, e.g., the $D = 2$ square lattice at half filling has a square-shaped Fermi surface. Below we provide some expressions for the $\langle d^\dagger c_r \rangle$ correlator for $D > 1$ assuming a circularly/spherically symmetric Fermi surface.

For an isotropic Fermi surface, we linearize the dispersion around the Fermi surface,

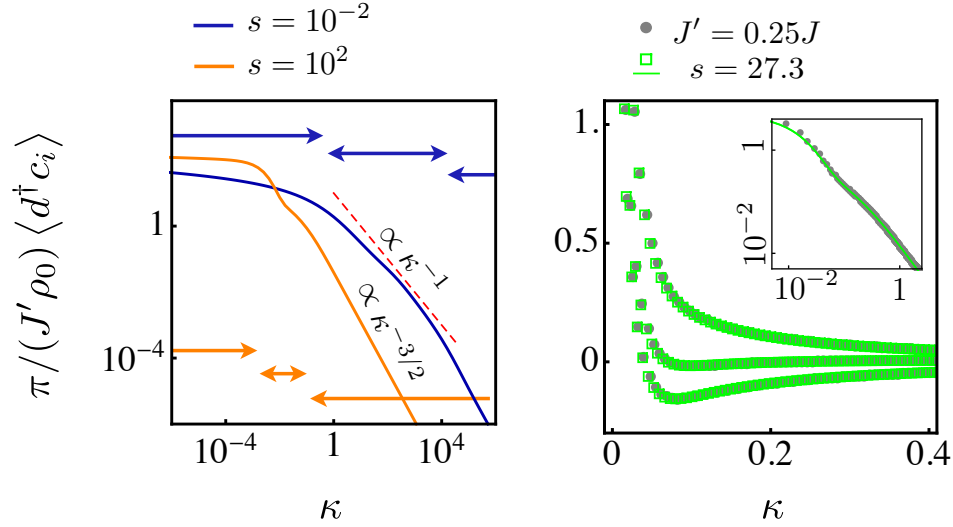


Figure 9. Screening cloud for bath with diverging density of states, case (b) of Fig. 8. Left: Envelope of $\langle d^\dagger c_i \rangle$ plotted against the scaled distance κ , using Eq. (16). A small s (blue/dark-solid) and a large s (orange/light-solid) case is shown. The different scaling regions are indicated by arrows near the top (for $s = 10^{-2}$) and bottom ($s = 10^2$) of the panel. Right: correlator $\langle d^\dagger c_i \rangle$ for the H_{NN} Hamiltonian with $J = -J_{NN} = 1$ and $J' = 0.25J$, compared with Eq.(16) with corresponding value $s \approx 27.3$. In the main panel, the full oscillatory behaviour is shown and not just the envelope. The inset shows a comparison of the envelope.

$\mathbf{k} = \mathbf{\Omega}(k_F + \varepsilon/v_F)$, with $\mathbf{\Omega}$ a D -dimensional unit vector. Eq.(5) then yields

$$\begin{aligned} \langle dc_r^\dagger \rangle \simeq & -J' \frac{k_F^{D-1}}{(2\pi)^D v_F} \int_{-\Lambda}^{\Lambda} d\varepsilon \int d^{D-1}\Omega \int d\nu \times \\ & A_{dd}(\nu) \exp \left[-i \left(k_F + \frac{\varepsilon}{v_F} \right) \mathbf{\Omega} \cdot \mathbf{r} \right] \frac{n_f(\nu) - n_f(\varepsilon)}{\nu - \varepsilon} \end{aligned} \quad (18)$$

Here Λ denotes a high-energy cutoff of the order of the bandwidth.

The explicit form of resonant level spectral function, $A_{dd}(\nu)$ given in Eq.(7), remains unchanged except for the modification of the density of states at the Fermi level $\rho_0 = \frac{k_F^{D-1}}{v_F(2\pi)^D} \mathcal{A}_{D-1}$ where $\mathcal{A}_{D-1} = \frac{2\pi^{\frac{D}{2}}}{\Gamma(\frac{D}{2})}$ is the area of the S_{D-1} sphere. Performing the angular integration and simplifying the previous expression using the explicit form of $A_{dd}(\nu)$ one obtains

$$\langle dc_r^\dagger \rangle \simeq -J' \rho_0 \int_{-\tilde{\Lambda}}^{\tilde{\Lambda}} du \frac{h_D[(\tilde{\epsilon}_F + u)\kappa] + (u - \tilde{\epsilon}_d) g_D[(\tilde{\epsilon}_F + u)\kappa]}{[(u - \tilde{\epsilon}_d)^2 + 1] (1 + e^{\tilde{\beta}u})} \quad (19)$$

where $\tilde{\Lambda} = \Lambda/\Gamma$ and $\tilde{\epsilon}_F = \epsilon_F/\Gamma$. The functions g_D and h_D are defined as

$$g_D(y) = (\mathcal{A}_{D-1})^{-1} \int d^{D-1}\Omega \exp[-i\mathbf{\Omega} \cdot \mathbf{e}_1 y] \quad (20)$$

$$h_D(y) = (\mathcal{A}_{D-1})^{-1} \int d^{D-1}\Omega \exp[-i\mathbf{\Omega} \cdot \mathbf{e}_1 y] \text{sgn}(\mathbf{\Omega} \cdot \mathbf{e}_1) \quad (21)$$

with \mathbf{e}_1 a fixed unit vector. Specifically, for $D = 2$ one obtains $g_2(y) = J_0(y)$ and $h_2(y) = H_0(y)$, respectively the Bessel and Struve functions of order zero. For $D = 3$,

$g_3(y) = \frac{\sin(y)}{y}$ and $h_3(y) = \frac{[1-\cos(y)]}{y}$. For $D = 1$, the integrals (20,21) become sums over the Fermi points, yielding $g_1(y) = \cos(y)$, $h_1(y) = \sin(y)$; using these expressions one recovers the on-dimensional solution treated in the previous sections.

At zero temperature and for $\tilde{\epsilon}_d = 0$, Eq.(19) simplifies to $\langle d^\dagger c_r \rangle = \frac{J' \rho_0}{\pi} T(\kappa)$ with

$$T(\kappa) = -\pi \int_{-\tilde{\Lambda}}^0 du \frac{h_d[(\tilde{\epsilon}_F + u)\kappa] + u g_d[(\tilde{\epsilon}_F + u)\kappa]}{[u^2 + 1]}. \quad (22)$$

In the $d = 1$ case the oscillatory part of Eq.(22) factors out, and the cutoff Λ can be sent to infinity in the remaining expression. In the $D > 1$ cases, unfortunately, this simplification does not occur except for the limit $\kappa \rightarrow \infty$. Since the cutoff Λ is of the same order as the Fermi energy ϵ_F which remains within the integral, it is not consistent to use $\Lambda \rightarrow \infty$. Treating the integral numerically, we have verified that the large-distance behavior (outside the screening cloud, $\kappa \gg 1$) is $T(\kappa) \sim \kappa^{-1}$ for $D = 2$ and $D = 3$, as it is for the $D = 1$ case. The long-distance behavior reflects an intrinsic property of the Fermi gas, so this is expected. However, the short-distance behavior (within the screening cloud, $\kappa \ll 1$) is cutoff-dependent and it is difficult to infer a general behavior. In addition, it should be borne in mind that angular dependence of the Fermi surface, which we have ignored, may also contribute to making the behavior of $\langle d^\dagger c_r \rangle$ non-universal.

9. Discussion; Open issues

To summarize, we have characterized the spatial structure of the impurity screening cloud for the resonant level model, using the impurity-bath two-point correlator $\langle d^\dagger c_x \rangle$ and the entanglement entropy S_l of a region surrounding the impurity with the rest of the system. Focusing on 1D baths, we have found that the behavior of the correlator $\langle d^\dagger c_x \rangle$ is found to be logarithmic ($\sim -\ln x$) within the cloud and power-law ($\sim x^{-1}$) outside the cloud. The analytic expression in the continuum limit wide-band approximation is provided in integral form for arbitrary temperatures [Eq. (9)]. The crossover occurs at a length scale ξ which varies as an inverse square with the coupling J' . The $\langle d^\dagger c_x \rangle$ envelopes calculated from finite-size lattices with different values of J' reproduce well the full analytical prediction through a scaling collapse of data. We have also shown the effect of impurity detuning ϵ_d from the Fermi energy. The screening cloud is robust for small detunings, but at larger detuning it gets destroyed by a new intermediate-distance regime that grows in spatial extent with the detuning.

The long-distance $\sim x^{-1}$ behavior for any D can be understood as the behavior of the two-point correlator of the undisturbed Fermi gas. Since the impurity is screened at large distances, this correspondence is expected. In the external impurity case, this behavior is obtained if $\langle d^\dagger c_x \rangle$ is calculated perturbatively in J' . In contrast, the short-distance $\sim -\ln x$ behavior cannot be explained in the same way. We are not aware of alternate arguments or derivations of the logarithmic behavior.

It is interesting to contrast the $\sim -\ln x$ to $\sim x^{-1}$ crossover with the isotropic Kondo model, in which case a crossover from $\sim x^{-1}$ to $\sim x^{-2}$ has been reported for

spin-spin correlators [15]. Our results for the RLM also provide definite predictions for the screening cloud of the single-impurity Anderson model, when described by two-point impurity-bath correlators. Some available numerical data is consistent with this prediction, but a thorough exploration of the SIAM screening cloud using various correlators is clearly necessary.

In addition to the standard RLM, we have presented results for the screening cloud with more complicated Fermi surface topology, as can be realized with next-nearest-neighbor couplings in the tight-binding bath. An intriguing case arises when part of the Fermi surface disallows linearization because the dispersion curves touches the chemical potential without crossing it; the divergent density of states leads to a non-Fermi-liquid behavior, namely, a power-law ($\sim x^{-3/2}$) decay at large distances with exponent $\neq 1$. It is remarkable that such unconventional physics can be generated from free-fermion systems.

Acknowledgments

MH thanks I. Affleck, E. Boulat and M. Garst for useful discussions. The authors also thank F. Assaad and F. Goth for help with the data of Ref. [13].

Appendix A. One-particle Green's function derivation

We present here the explicit analytical calculation for external RLM leading to Eq.(8). Similar results can be obtained for the other two geometries. We also show that Eq.(5) is valid even in the presence of interactions at the impurity site.

At finite temperature, the imaginary-time single-particle Green's function are given by

$$G(\tau) = \begin{pmatrix} G_{cc}(\tau) & G_{cd}(\tau) \\ G_{dc}(\tau) & G_{dd}(\tau) \end{pmatrix} \quad (\text{A.1})$$

with $\langle \dots \rangle$ the thermal average with respect to the Gibbs ensemble with Hamiltonian H_{ext} and where $G_{cc}(\tau)$, $G_{cd}(\tau)$, $G_{dc}(\tau)$ and $G_{dd}(\tau)$ (a $\mathcal{L} \times \mathcal{L}$ matrix, a column vector, a line vector and a c-number respectively) are defined by

$$[G_{cc}(\tau)]_{i,j} = \langle T_\tau c_i(\tau) c_j^\dagger(0) \rangle \quad (\text{A.2})$$

$$[G_{cd}(\tau)]_i = \langle T_\tau c_i(\tau) d^\dagger(0) \rangle \quad (\text{A.3})$$

$$[G_{dc}(\tau)]_i = \langle T_\tau d(\tau) c_i^\dagger(0) \rangle \quad (\text{A.4})$$

$$G_{dd}(\tau) = \langle T_\tau d(\tau) d^\dagger(0) \rangle. \quad (\text{A.5})$$

These definitions extend to the other two geometries, and also to the interacting cases. (For the Anderson model the additional spin index has to be taken into account, however off diagonal correlations in spin index vanish identically by spin conservation).

Assuming that interactions arise only at the impurity site, Dyson's equation in Matsubara space, takes the form

$$G_{dd}^{-1}(i\omega_n) = G_{0,dd}^{-1}(i\omega_n) - \Sigma_{dd}(i\omega_n) \quad (\text{A.6})$$

$$G_{dc}(i\omega_n) = -G_{dd}(i\omega_n)V G_{0,cc}(i\omega_n) \quad (\text{A.7})$$

$$G_{cc}(i\omega_n) = G_{0,cc}(i\omega_n) + G_{0,cc}(i\omega_n)V^\dagger G_{dd}(i\omega_n)V G_{0,cc}(i\omega_n) \quad (\text{A.8})$$

and thus the problem is reduced to finding the explicit form of $G_{dd}(i\omega_n)$. Here $G_{0,cc}$ and $G_{0,dd}$ are the single-particle Green's function of the conduction electron bath and impurity site respectively in absence of tunneling between the two (*i.e.* $J' = 0$)

$$[G_{0,cc}(i\omega_n)]_{i,j} = \sum_k \frac{e^{ik(r_i - r_j)}}{i\omega_n - (\epsilon_k - \mu)} \quad (\text{A.9})$$

$$G_{0,dd}(i\omega_n) = \frac{1}{i\omega_n - (\epsilon_d - \mu)} \quad (\text{A.10})$$

with ϵ_d is the energy of the impurity level and μ is the chemical potential of the bath, and V is a line vector with entries $[V]_i = -J'\delta_{i,0}$.

Eq.(5) can be obtained from Eq.(A.7) noting that $\langle d^\dagger c_i \rangle = -G_{dc}(\tau = 0^-)$ and by using the spectral decomposition of the impurity Green's function $G_{dd}(i\omega_n) = \int d\nu \frac{A_{dd}(\nu)}{i\omega_n - \nu}$, where $A_{dd}(\nu) = -1/\pi \text{Im} [G_{dd}(\omega + i0^+)]$ is the impurity spectral function.

For the external RLM the self-energy of the d electrons acquires the simple form

$$\Sigma_{dd}(i\omega_n) = V G_{0,cc}(i\omega_n) V^\dagger \quad (\text{A.11})$$

In the large \mathcal{L} limit using the approximation $\frac{1}{\mathcal{L}} \sum_k \dots \rightarrow \int d\nu \rho(\nu) \dots$ and assuming a constant density of states $\rho(\nu) \simeq \rho_0 \Theta(\Lambda - |\nu - \mu|)$ around the Fermi level, one obtains, in the wide band limit $\nu \ll \Lambda$, $\Sigma_{dd}(i\omega_n) \simeq -i \text{sign}(\omega_n) \Gamma$ with $\Gamma = \pi J'^2 \rho_0$. This result together with Eq.(A.6) yields the expression of the spectral function of the d level used in the main text.

In the case of Fig.8, where the dispersion relation touches the Fermi energy without crossing it, the impurity self-energy, for energies much smaller than the bandwidth, is given by:

$$\Sigma_{dd}(i\omega_n) = -i \text{sign}(\omega_n) \Gamma + \frac{\delta}{\sqrt{i\omega_n}},$$

with $\delta = \frac{J'^2}{2\sqrt{a_F}}$ and where a_F is obtained by expanding the dispersion relation about the critical Fermi momentum (here assumed to arise for $k = 0$) $|\epsilon_k - \mu| \simeq a_F k^2$. $\Gamma = \pi J'^2 \rho_0$ is given as before with $\rho_0 = |\pi v_F|^{-1}$ being the regular part of the density of states. The corresponding impurity spectral function is given by:

$$A_{dd}(\nu) = \begin{cases} \frac{1}{\pi} \frac{\Gamma}{(\nu + \frac{\delta}{\sqrt{\nu}})^2 + \Gamma^2} & \text{for } \nu > 0 \\ \frac{1}{\pi} \frac{\Gamma + \frac{\delta}{\sqrt{\nu}}}{\nu^2 + (\Gamma + \frac{\delta}{\sqrt{\nu}})^2} & \text{for } \nu < 0 \end{cases} \quad (\text{A.12})$$

References

- [1] J. Kondo, Prog. Theo. Phys. **32**, 37 (1964).
- [2] A. C. Hewson, *The Kondo Problem to Heavy Fermions* (Cambridge University Press, New York, 1993).
- [3] P. W. Anderson, Phys. Rev. **124** 41 (1961).
- [4] P. Schlottmann, Phys. Rev. B **22**, 613 (1980); **25**, 4815 (1982). V. M. Filyov, A. M. Tzvelik, and P. B. Wiegmann, Phys. Lett. A **81**, 175 (1980).
- [5] E. Boulat, H. Saleur, and P. Schmitteckert, Phys. Rev. Lett. **101**, 140601 (2008).
- [6] I. Affleck and P. Simon, Phys. Rev. Lett. **86**, 2854 (2001).
- [7] P. Simon and I. Affleck, Phys. Rev. B **64**, 085308 (2001).
- [8] P. Simon and I. Affleck, Phys. Rev. Lett. **89**, 206602 (2002).
- [9] P. Simon and I. Affleck, Phys. Rev. B **68**, 115304 (2003).
- [10] T. Hand, J. Kroha, and H. Monien, Phys. Rev. Lett. **97**, 136604 (2006).
- [11] C. A. Büsser, G. B. Martins, L. Costa Ribeiro, E. Vernek, E. V. Anda, and E. Dagotto, Phys. Rev. B **81**, 045111 (2010).
- [12] J. Simonin, arXiv:0708.3604.
- [13] F. Goth, D. J. Luitz, and F. F. Assaad, arXiv:1302.0856
- [14] A. Holzner, I.P. McCulloch, U. Schollwck, J. von Delft, and F. Heidrich-Meisner, Phys. Rev. B **80**, 205114 (2009).
- [15] L. Borda, Phys. Rev. B **75**, 041307(R) (2007).
- [16] L. Borda, M. Garst, and J. Kroha, Phys. Rev. B **79**, 100408(R) (2009).
- [17] I. Affleck, L. Borda, and H. Saleur, Phys. Rev. B **77**, 180404(R) (2008).
- [18] A. K. Mitchell, M. Becker, and R. Bulla, Phys. Rev. B **84**, 115120 (2011).
- [19] E. S. Sørensen, M. S. Chang, N. Laflorencie, and I. Affleck, J. Stat. Mech.: Theory Exp. (2007) P08003; (2007) L01001.
- [20] A. Bayat, P. Sodano, and S. Bose, Phys. Rev. B **81**, 064429 (2010).
- [21] V. Barzykin and I. Affleck, Phys. Rev. B **57**, 432 (1998).
- [22] H. Ishii, J. Low Temp. Phys. **32**, 457 (1978).
- [23] E. S. Sørensen and I. Affleck, Phys. Rev. B **53**, 9153 (1996).
- [24] F. D. M. Haldane, J. Phys. C **11**, 5015 (1978). R. Zitko, J. Bonca, A. Ramsak, and T. Rejec, Phys. Rev. B **73**, 153307 (2006).
- [25] G. Toulouse, Phys. Rev. B **2**, 270 (1970).
- [26] A. Schiller and S. Hershfield, Phys. Rev. B **58**, 14978 (1998). K. Joho, S. Maier, and A. Komnik, Phys. Rev. B **86**, 155304 (2012).
- [27] D. Lobaskin and S. Kehrein, Phys. Rev. B **71**, 193303 (2005). M. Heyl and S. Kehrein, J. Phys.: Cond. Matt. **22**, 345604 (2010).
- [28] M. Medvedyeva, A. Hoffmann, and S. Kehrein, arXiv:1307.5488.
- [29] R. Vasseur, K. Trinh, S. Haas, and H. Saleur, Phys. Rev. Lett. **110**, 240601 (2013).
- [30] T. Posske, C.-X. Liu, J. C. Budich, and B. Trauzettel, Phys. Rev. Lett. **110**, 016602 (2013).
- [31] S. Eggert and I. Affleck, Phys. Rev. B **46** 10866 (1992).
- [32] H. Saleur, P. Schmitteckert, and R. Vasseur, Phys. Rev. B **88**, 085413 (2013).